Available online at www.sciencedirect.com
ScienceDirect
Deep-Sea Research II 55 (2008) 338–350
DEEP-SEA RESEARCH PART II
www.elsevier.com/locate/dsr2

Springtime ice motion in the western Antarctic Peninsula region

Cathleen A. Geiger[a,b,*], Donald K. Perovich[a]

[a]Snow and Ice Branch, Cold Regions Research and Engineering Laboratory, Hanover, NH, USA
[b]Center for Climatic Research, University of Delaware, Newark, DE, USA

Accepted 4 November 2007
Available online 27 December 2007

Abstract

Oscillatory motion of sea-ice is examined using two ice-drifting buoys separated by 1° latitude near 66°S during the winter to spring transition in the Marguerite Bay region west of the Antarctic Peninsula. The buoys' motions exhibit spectrally distinct periods (12.87 ± 0.04 and 13.03 ± 0.04 h, respectively) despite highly correlated motion between them (r^2 is 0.62 and 0.81 for u and v, respectively). The periods shift with latitude and nearly match the local inertial periods (13.00 and 13.10 h, respectively). The oscillations are further examined with respect to the kinematics involved in the breakup process of sea-ice. These include hourly resolved manifestations of circular trajectories, semi-circular oscillations with compressed trajectory cusps, and "accordion-like" compressions along straight-line trajectories. Oscillations are found in all trajectory types over the lifetime of both buoys (several months). Traditional circular and semi-circular oscillations are particularly prominent during two episodes, one of which is preceded by strong wind events and a substantial decrease in ice thickness and concentration. These episodes combine with seasonally warming temperatures to break up and melt the sea-ice cover. We discuss potential relationships between the degradation of the ice pack during spring breakup and the increase in energy at near-inertial frequencies including the appearance of a non-linear cascade of energy within the ice from the low frequencies (commensurate with storms and fortnightly tides) to semi-diurnal frequencies. We further comment on the implications this type of high-frequency motion has on local biological ecosystems. Specifically, we find that sea-ice semi-diurnal oscillations are at their peak during the final decay of sea-ice just before springtime primary productivity begins. Hence, the oscillatory motion of sea-ice not only serves as an effective mixing agent within the ice–ocean mixed layer, but also serves as an effective seeding platform for distributing phyto- and zooplankton overwintering within and around the ice floes.

Keywords: Sea-ice kinematics; Inertial oscillations; Spring breakup

1. Introduction

Ice motion impacts vertical heat and vapor exchange between the atmosphere and ocean. It also contributes to mixing in the upper ocean, which affects ice thickness and morphology. These processes influence biological activity in and under the ice as well as chemical pathways. In this paper, we focus on the mixing mechanisms of sea-ice on hourly to daily time scales during the winter-to-spring transition of sea-ice. This work is complementary to the open water drifter results from the Southern Ocean Global Ocean Ecosystem Dynamics (SO GLOBEC) as described by Beardsley et al. (2004) during this same time period.

Hunkins (1967) points out that inertial oscillations in sea-ice are caused by the earth's rotation acting on the center of mass of individual ice floes as they move in rigid body motion at the air–sea interface. His seminal work on inertial oscillations of the drifting T3 tabular iceberg island in the high Arctic provides both the observational and theoretical framework for inertial oscillations of sea-ice. He shows that the mathematical relationship for inertial oscillations is primarily between the inertial term, wind forcing, Coriolis, and some form of damping. The ocean surface mixed layer develops inertial oscillations in a similar way (Pond and Pickard, 1983) albeit as a fluid mass.

Tidal oscillations are phenomenologically distinct from inertial oscillations. Tides are created by the gravitational

*Corresponding author. Now at Department of Geography, University of Delaware, 216 Pearson Hall, Newark, DE, USA. Tel.: +1 603 646 4851; fax: +1 603 646 4644.
E-mail address: cgeiger@udel.edu (C.A. Geiger).

0967-0645/$ - see front matter © 2007 Elsevier Ltd. All rights reserved.
doi:10.1016/j.dsr2.2007.11.008

force between large astronomical bodies such as the sun and moon acting on large earthly bodies like seas and oceans. Sea-ice sits upon the water that is responding to tidal forces. As a result, sea-ice experiences very little tidal force directly, and instead, it responds to tides through a momentum transfer from ocean tidal currents to the ice.

Colony and Thorndike (1980) explain that higher-frequency surface motion, including inertial- and tidal-derived motions, cannot be explained by a linear model forced by the wind. Their findings show a high coherency between ice floes separated hundreds of kilometers away at both low and high frequency even though the wind is only correlated at low frequencies across great distances. They conclude that the elastic property of ice allows for the high-frequency coherency as a function of the resistance to horizontal deformation. McPhee (1978) successfully models inertially derived sea-ice motion and concludes that the inertial term of the momentum balance makes a significant contribution to the total air–ice–sea momentum transfer especially above daily frequencies. He also discusses the relationship between ice concentration and the extent of inertial oscillations by noting that the summer free-drift state is ideal for inertial oscillation development while in winter, where the ice is more of a rigid-lid, these motions are substantially dampened. McPhee (1978) discusses that such oscillations must contribute substantially to the development of new ice production during the freeze-up period.

Work by Geiger et al. (1998a, b) and Geiger and Drinkwater (2005) confirm the importance of shorter-period motion (less than daily period) with regard to deep water formation in the Weddell Sea, where semi-diurnal tidal and inertial frequencies are resonant and generate strong kinematic motion. Findings in Geiger and Drinkwater (2005) confirm original discussions by Foldvik and Gammelsrød (1990) by demonstrating how hourly- to daily-period motion substantially contributes to high bottom-water production rates because of the non-linear fluxes that develop over time scales of hours. Hourly integrated heat and salt flux rates are found to be twice as high as those computed using only longer (greater than daily period) motions and forcing (Geiger and Drinkwater, 2005).

Returning to the issue of inertial oscillations, Heil and Hibler (2002) assert that inertial power in the ice is not due to high-frequency forcing of the wind or the water; rather they claim that high-frequency motion is generated by the ice because of changes in the wind speed and direction, ice interaction, and changes in ice thickness characteristics. This combination is believed to modify both the magnitude and phase of the inertial oscillation. They, like Geiger and Drinkwater (2005), hypothesize that there is a cascade of energy from lower to higher frequencies within the ice due to non-linear ice dynamics. Heil and Hibler (2002) also believe that an energy cascade collects and becomes trapped at the inertial period as a resonance effect.

In the Arctic, Kwok et al. (2003) show persistent oscillatory sea-ice motion that they determine to be inertial through careful analysis of the rotation of strain-rate ellipses moving in the direction of an inertial ellipse. Their main emphasis is to show how important these ubiquitous inertial oscillations are to new ice production within the recurring open water fractions at each inertial cycle. These results concur with findings found in the Weddell Sea in the Antarctic (Geiger and Drinkwater, 2005) and further support the universal presence of strong ubiquitous inertial signals in ice drift in both hemispheres. This is an important connection given several distinct differences between Arctic and Antarctic sea-ice properties and processes (Ackley and Weeks, 1990).

In the high Arctic, where inertial fluctuations rotate clockwise while tidal fluctuations predominantly rotate counterclockwise, rotary spectra can be used to separate tidal and inertial fluctuations (Hibler et al., 2006). Hibler et al. (2006) believe that numerical models (ranging from process models to fully coupled air–ice–ocean models) are needed to resolve the underlying causality of the oscillation sources in both the Arctic and Antarctic.

The geophysics just presented also has a significant impact on the survival of local biological species. As discussed in the review paper by Ackley and Sullivan (1994), the few biological species that do survive within the polar seas have adapted to the form, evolution, and deterioration processes of sea-ice and its annual cycle. From a biological perspective, sea-ice and its diverse forms serve as a range of habitats of different sizes, salinities, temperatures, and nutrients. The microstructure and brine channels are ideal for the smallest species as is the interface between the snow and ice. Larger chambers formed from the ice blocks of pressure ridges are sufficient to house Antarctic krill (*Euphasia superba*) and small fishes. Additionally, the roughness of the sea-ice bottom (especially of ridges) provides a floating, semi-translucent platform for species to over-winter. These basic infrastructures allow a multi-trophic biological community to thrive within and around sea-ice. This is an important biophysical coupling which has received little attention to date.

In austral spring, when the first rays of light begin to return, the translucence of sea-ice allows phytoplankton trapped within the floes to start growing again. As pointed out by Smith et al. (2000), the carbon uptake in biological species increases rapidly in the spring with a maximum in carbon uptake about 4 weeks earlier than biomass maximum production. The current hypothesis is that irradiance is the limiting agent to growth in the spring (Smith and Gordon, 1997) while nutrients are the limiting agent to sustained growth in summer (Sedwick and DiTullio, 1997).

The Marguerite Bay region located just west of the Antarctic Peninsula is characterized by an abundant population of Antarctic krill and is believed to be an area that supports successful overwintering of this species (Hofmann et al., 2004). Howard et al. (2004) identify one of the critical physical processes necessary to sustain the rich nutrient source, namely, strong near-inertial baroclinic waves responsible for sustaining a shear zone at the sharp pycnocline at the base of the mixed layer. They claim that

this physical feature sustains a strong upward diapycnal flux of salt, heat, and nutrients from the Upper Circumpolar Deep Water (UCDW) into the surface-mixed layer. Hence, there are a number of important regional biophysical coupled processes being resolved through the SO GLOBEC field program that are key to understanding, modeling, and predicting biomass balances specifically within the Marguerite Bay region.

In this paper, we focus on the behavior of observed sea-ice oscillations from the SO GLOBEC cruise in 2002. A critical topic not covered in the literature above is the contribution of inertial and/or tidal oscillations to the winter–spring transition state of sea-ice and the contribution of these oscillations to biological productivity, especially when the ice is changing from a rigid-lid approximation to a highly diffuse free-drift state. We explore this particular transition period using observations from Marguerite Bay near 66°S. This region is very useful for discussions of tidal-inertial fluctuations because it is located farther equatorward from tidal-inertial resonance latitudes relative to many other locations having an annual sea-ice cover.

2. Observations

The central data for this paper are the autonomous GPS time series from two buoys deployed on sea-ice during the SO GLOBEC experiment in 2002 in Marguerite Bay, Antarctica. The buoys are designed to investigate ice motion, surface air temperature and pressure, and the mass balance of the ice cover. Buoy 1 (referred to as the inner buoy in all figures because it is located further south and deeper in the pack ice) was installed on 23 August 2002 at 66.742°S, 72.2055°W. The buoy reported GPS position, barometric pressure, and air temperature. It operated from its installation in August 2002 until the ice melted in January 2003.

Buoy 2 (referred to as the outer buoy in all figures because it is located further north and closer to the ice edge) was installed on 3 September 2002 at 66.742°S, 72.2055°W. This was an ice-mass balance buoy. This buoy also reported barometric pressure, GPS position, and air temperature. In addition, it had a thermistor string that measured a vertical profile of temperature, at 10 cm spacing, from the air, through the snow and ice, and into the upper ocean. There were acoustic sensors measuring the positions of the snow surface and ice bottom to determine snow depth and ice thickness. It operated from installation until 5 December 2002. The buoy data were transmitted via ARGOS telemetry back to Hanover, NH, where it was processed and reduced.

Critical auxiliary data include hourly wind speed and direction, atmospheric pressure, and air temperature. These data are available from the nearest meteorological station, Rothera, through the British Antarctic Survey Meteorological Office (2005). Fig. 1 provides a good overview of typical distances between the buoys, relative

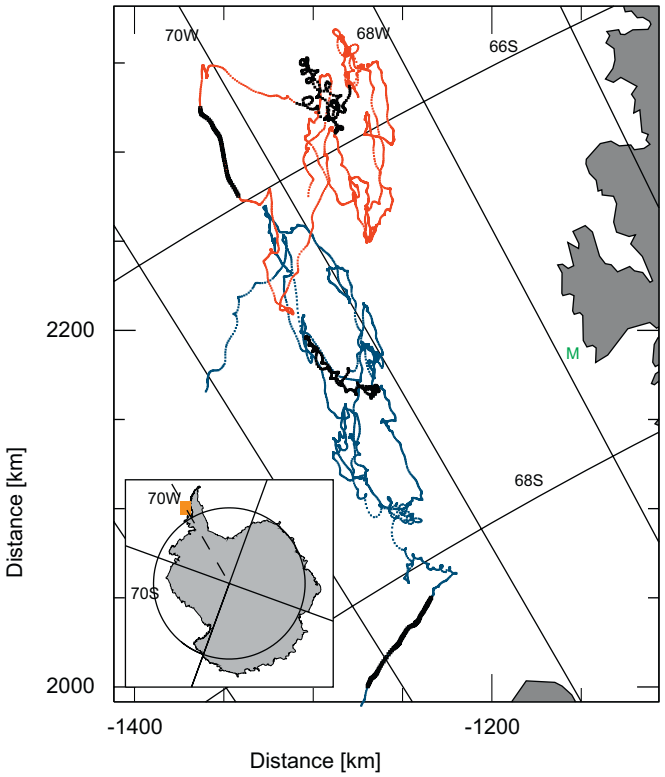

Fig. 1. Overview of buoy trajectories. Buoy 1 (ARGOS ID 07948—inner buoy) and buoy 2 (ID 07413—outer buoy) drifters are located on sea-ice floes with GPS receivers. Buoy 1 located deeper in the pack where sea-ice concentration is about 10% higher on average than Buoy 2. Nearest meteorological station (Rothera) is identified with bold green M on the Antarctic Peninsula. Drift track oriented relative to 40°W parallel to the coastline. Thicker black trajectories provided as a cross-reference for Fig. 6.

to each other, and in relation to Rothera. Buoy distances to Rothera ranged from 100 to 250 km. Finally, 25-km resolution sea-ice concentration were derived from NASA's daily passive microwave from the Special Sensor Microwave Imager (SSM/I) system using the bootstrap algorithm (http://nsidc.org/data/docs/daac/nsidc0079_bootstrap_seaice.gd.html) have been downloaded from the National Snow and Ice Data Center (NSIDC, 2005).

3. Data processing

3.1. Computation of buoy and wind velocity

Latitude and longitude buoy positions are projected onto the polar stereographic SSM/I grid, with 70°S chosen as the reference latitude (plane of no distortion) and an eccentricity for the earth's surface shape of $e = 0.08181615$. This is a range and bearing conserving projection and, therefore, ideally suited for buoy analysis. An initial investigation reveals the dominant drift track oriented parallel to the coast. A reference longitude of 40°W yields a projection with the y-axis oriented parallel to the coast, which is oriented 30° clockwise from a true N–S orientation. We choose this orientation (as will be seen in the drift

statistics presented ahead) to resolve buoy drift components parallel and perpendicular to the nearby coastline and aligning coastal current. The data are recorded hourly with no data gaps in excess of a couple of hours. A simple linear interpolation is therefore sufficient for determining hourly positions. Data quality is controlled using a simple forward difference velocity with a threshold for velocity and velocity change of 50 and 20 cm s^{-1}, respectively, to flag questionable data. Centered differencing of interpolated positions is used to compute the final velocity, with flagged velocities marked as undefined. The hourly wind speed at the Rothera station is converted from knots to m s^{-1} and transformed into *u*- and *v*-components with the same orientation as the buoys (i.e. normal and tangential to the coastline).

We also wish to separate low and high frequency for each velocity component, so we add a 10% reflected signal at the ends in preparation for filtering to avoid edge effects (this edge signal is removed after filtering). We send the drift and wind velocity components through a 37-h infinite impulse response filter as recommended by Roberts and Roberts (1978) to isolate signals longer than a 1-day period for comparison of low-frequency components in the wind and ice motion. Using the full spectrum of the signals, trajectories of selected segments are isolated to examine the drift behavior of buoys during high-rotational and high-translational sequences.

3.2. Spectral methods

Conventional Fast Fourier Transform (FFT) periodogram spectral methods account for all the spectral energy within chosen frequency bins but are limiting when one wishes the precise frequency of a specific peak. The maximum entropy method (MEM) is the preferred approach for finding peaks with a relatively high degree of precision. Also known as the autoregressive power spectral density (AR PSD) model, MEM assumes that a process is random and stationary and can be represented in a closed form by a statistical model whose spectrum is a function of frequency. This autoregressive (AR) model is of order *p* which is the number of poles in the complex *z*-plane. Specifically, the spectral peaks are resolved at the poles (singularities) of a truncated Laurent series in the complex plane and represent a signal above a random process.

The details of the algorithm are explained, for example, by Press et al. (1990), and many standard signal-processing packages (e.g., MatLab, IDL, PV-wave, etc.) contain the needed routines. The main difficulty with MEM is determining which order of pole to use. For this study, we follow the recommendation made by Emery and Thomson (1997), who suggest the Akaike information criterion (AIC) as described in Lütkepohl (1985). Using these recommendations, we determine that the optimal number of poles is 81 for Buoy 1 and 117 for Buoy 2.

3.3. Processing of additional environmental data

The remaining environmental data are downloaded in a ready-to-use form, except for some small conversions for wind speed and sea-ice concentration. The wind speed and direction are recorded relative to compass bearings and transformed onto the SSM/I grid with a reference longitude of 70°W (local longitude). This result is rotated by 30° to orient them relative to 40°W. The negative of these values is used to orient the wind relative to the flow direction for comparison with ice drift. Daily sea-ice concentration from the gridded SSM/I products are extracted using a four-point weighted interpolation of nearest SSM/I pixels relative to the noon positions of each buoy. The temperatures are determined using a thermistor and have a resolution of 0.03 °C.

4. Results

We see in Fig. 1 two distinct types of motion in the buoy trajectories: (a) long trajectories of translational motion running primarily parallel to the coastline, and (b) compressed oscillatory motion moving in a north–south orientation. Evidence for strong translational motion along the coastline is isolated by binning the buoy speed and direction into 5 cm s^{-1} and 10° bins, respectively, and identifying the mode of the drift direction (Fig. 2). We are using a rectilinear coordinate system with the *y*-axis parallel to the coast. This axis is 30° clockwise from a true N–S orientation. The combined statistics from both buoys (black dashed line) shows a mode at $\pm 90°$ which is parallel to the coast. With the coast confining the ice motion to the east (and eventually from the south), trajectories around 90° represent motion in the north-by-northeastward direction toward the open sea, while trajectories around −90° are moving south-by-southwest, which we will call here the retreating direction or the direction of the retreating ice. The buoys are located on the shelf with the translational motion in agreement with detailed drift analysis by (Beardsley et al., 2004) using 24 drifting drogues and hydrographic results by Klinck et al. (2004).

The directional mode for each buoy is broader than the combined result and spans about 30° with the highest directional modes centered at +105° and −105° for the outer (closest to the ice edge) and inner (deep in the pack) buoys, respectively. The outer buoy has two peak modes, one at +105° and the next slightly smaller peak at −95°. These modes support the idea of oscillatory motion (flipping between plus and minus directions—Fig. 3) with the slightly larger mode in the positive direction supporting a slow divergent state (i.e. the ice near the ice edge is oscillating and diverging toward the ice edge). Contrary to this, the inner buoy (deeper in the pack ice) oscillates between −105° and +95° but has the more dominant mode in the retreating direction, suggesting motion near that buoy is also oscillating, but more damped with a strong retreating advective component.

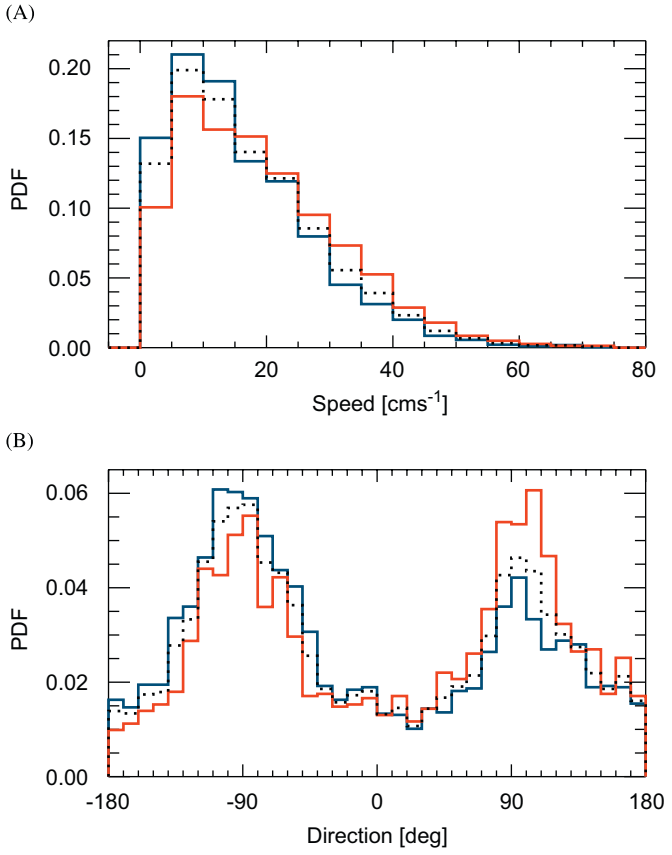

Fig. 2. Drift statistics. The probability distribution function (PDF) for drift speed (A) and direction (B) with bins of 5 cm s^{-1} and 10°, respectively. Buoy-coding corresponds with Fig. 1. Dotted line is PDF using both buoys combined. The direction is oriented such that ±90° is parallel to the coastline.

4.1. Springtime ice breakup processes

The statistical observations are well reflected in the final days of each buoy as they are exposed to ice breakup processes. In the case of the outer buoy (Fig. 1) at the start of ice-edge breakup, the buoy goes through one last oscillation cycle (highlighted in black in Fig. 1) followed by a southward translation. Dynamically, there is a strong storm starting on day 300 where low air pressure (Fig. 4A), warm air temperatures (Fig. 4B), and strong winds (Fig. 5) are moving across the region in a southeasterly direction (coming from the northwest), which initially compresses the ice edge toward the pack ice. This is the strongest recorded wind event of the buoys' lifetime and therefore a significant period of mechanical ice–ice interaction and kinematic motion (Fig. 3). We name this time period, from day 300 to 310, Event 1. There is also a warming in air temperature (Fig. 4B) and a notable change in both ice bottom ablation (Fig. 4C) and reduction in ice concentration (Fig. 4D). The ocean temperature rises and then falls again by 0.1 °C at the outermost buoy with water temperatures close to the freezing point (Fig. 4E). Near the end of Event 1, a second smaller low pressure system develops around day 310, though not as deep as the first (Fig. 4A). Again there is a strong, though less intense, southeasterly wind flow of shorter duration (Fig. 5). Evidence of declining ice concentration following Event 1 suggests that these two storms combined with increased seasonal warming are the initiators of ice breakup processes (including melting, advection, and ice floe decay) at the ice edge with significant damage to ice floes deep into

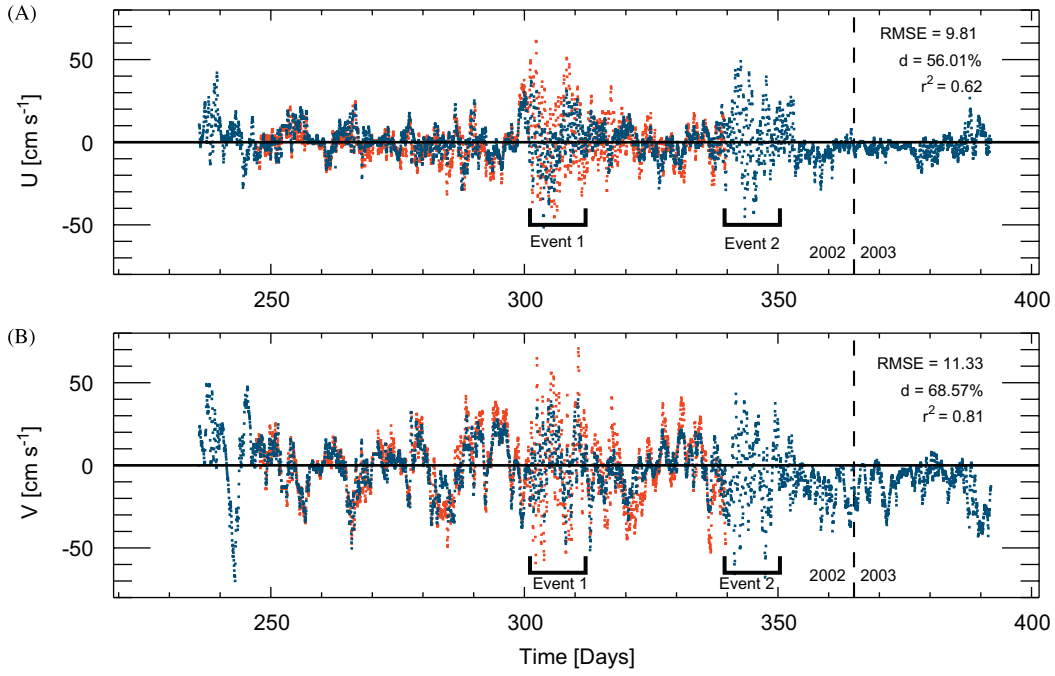

Fig. 3. Buoy drift signal. Using the same color scheme as previous figures, drift components shown normal (A) and tangential (B) relative to the coast. A strong oscillation event (Event 1) is captured by both buoys while a second event (Event 2) is captured by the longer surviving buoy. Root-mean-squared-error (RMSE), index of agreement (d), and correlation (r^2) provided as relevant statistics between buoys. Time is shown as day of the year relative to 2002 with vertical dashed bar denoting year change.

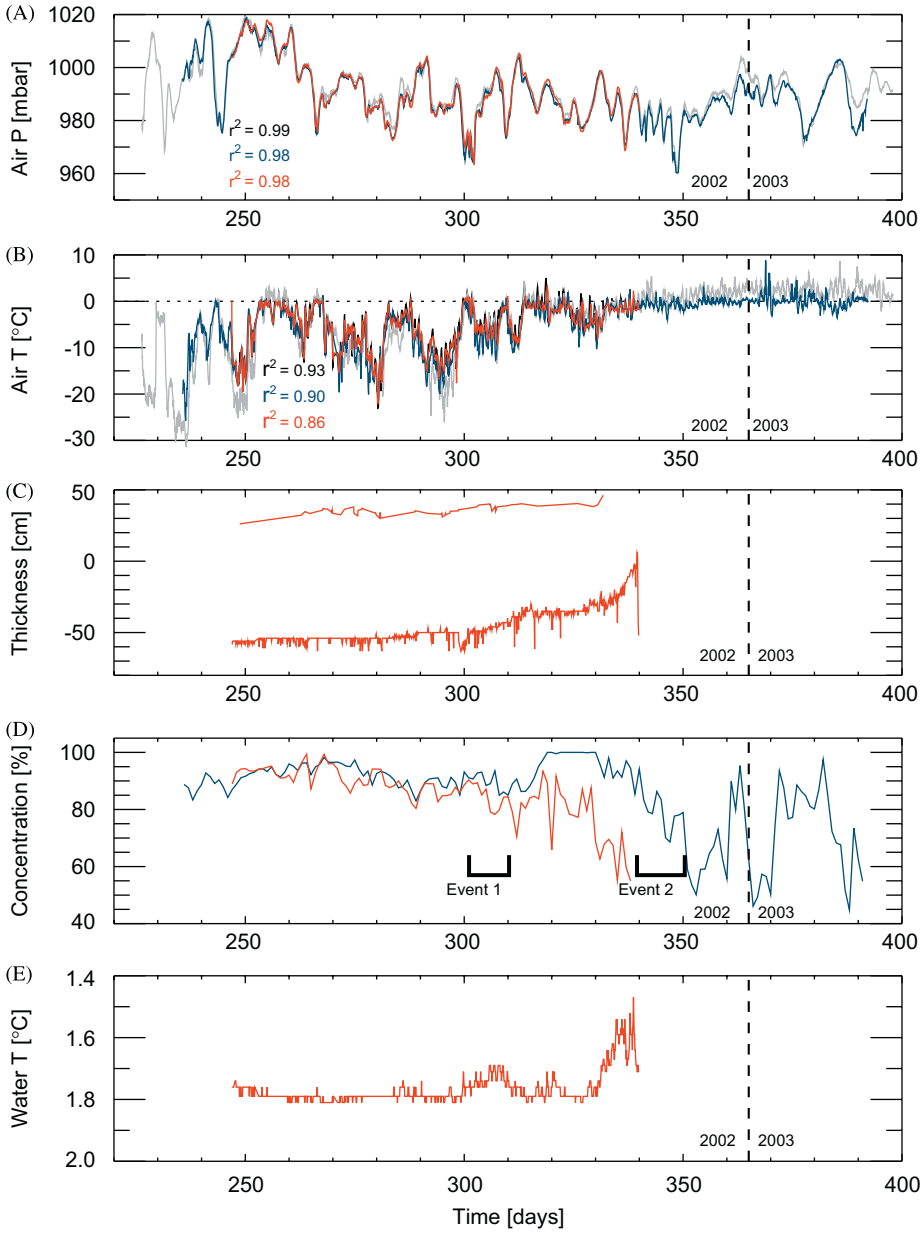

Fig. 4. Environmental variables. Time series from Rothera meteorological station longest time series and buoys using previous color scheme. Correlation (r^2) between buoys (black), between Buoy 1 and Rothera inner buoy, and between Buoy 2 and Rothera outer buoy also shown.

the pack ice as seen by the high kinematic activity of the interior buoy in Fig. 3 during Event 1. The final demise of the outer buoy results from a continual increase in bottom ablation (Fig. 4C) and a drop in ice concentration to $60 \pm 10\%$ (Fig. 4D). Essentially, the ice thins to the point where it no longer supports the buoy and data transmission ends. Increasing ocean heat flux and air temperatures (Figs. 4B and E) are the main thermodynamic contributors.

About a month later, starting on day 339 a similar high kinematic event occurs (Event 2, Fig. 3). This event begins just as the outermost buoy stops transmitting and is most likely the source of the demise of the ice floe supporting the outer buoy. There is another strong low-pressure system present at the start of Event 2 as seen in the low-frequency signal (Fig. 5). Throughout the 30-day period following Event 1, two additional pressure systems moved through with southwesterly flow as a pulsing input of momentum transfer over the sea-ice. Then, around day 320, the weather pattern changes with the winds flowing only modestly from the southwest and southeast off the continent. Additionally, there is a substantial increase in water temperature (Fig. 4E), thinning of ice (Fig. 4C), and decrease in ice concentration (Fig. 4D). This is first seen at the outer buoy around day 330 as the water temperature rises as much as 0.3 °C above freezing between days 330 and 339. These observations suggest that warming of ocean temperatures is occurring through a combination of the

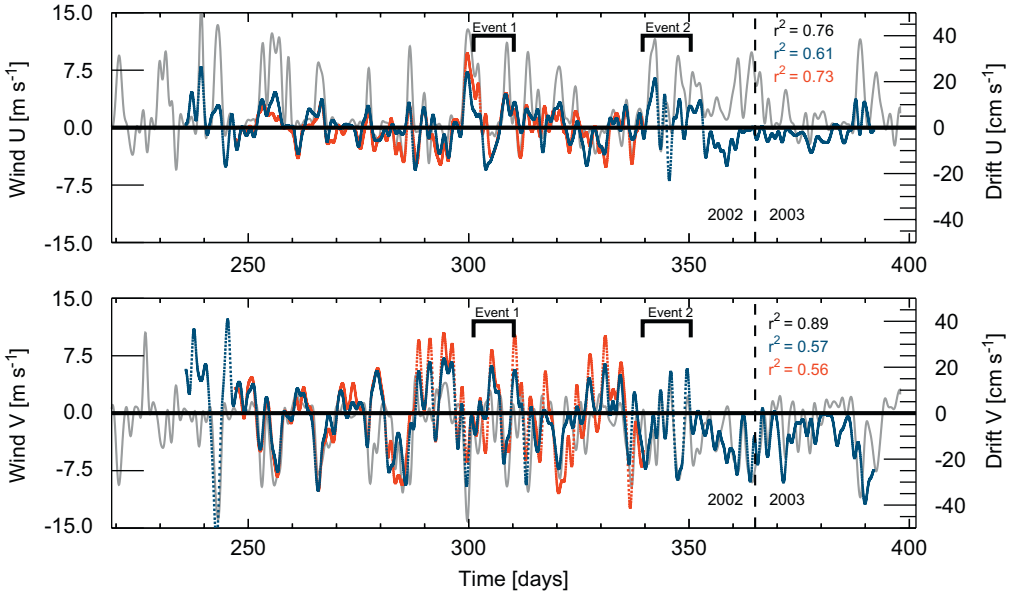

Fig. 5. Low-frequency signal. Using a 37-h Butterworth low-pass filter, the low-frequency component of wind and buoy drift shown using the same naming convention as previous figure. *Note*: the wind is shown in the drifting sense (i.e. direction of flow) with a 35° turning angle to compare with ice drift (details in text).

seasonal warming of the air temperature and high oscillatory ice motion in the presence of relatively mild wind conditions. The dominant processes between Events 1 and 2 include the warming of the upper water layers (which have a very low albedo) and oscillating ice motion (as a stirring mechanism). These processes are mechanisms that can enhance the melting process.

The buoy more interior in the ice pack (Fig. 1) goes through the same oscillatory motion during Event 1, but then continues, with an 11-day lag in ice concentration reduction, through a similar ice breakup processes until about day 350 (Fig. 4D). Then, a change of events occurs, and this remaining buoy experiences erratic ice concentrations varying from 45% to nearly 100% over the next 45 days with consistently warmer air temperatures (Fig. 4B) contributing to the final breakup process of the remaining ice pack.

4.2. Trajectory patterns

Looking more closely at the behavior of selected sections of the trajectories, we see in Fig. 6 (as highlighted in Fig. 1), that the two basic trajectory modes (translational and oscillatory) are both undergoing oscillatory motion with periods on the order of a half-day. During the "noisier" Events 1 and 2, the trajectories of the outer buoy are circular in shape. In Fig. 6A, there are also semi-circular trajectories separated by cusps containing multiple position measurements clustering together (which also give us confidence in the relative accuracy of the GPS). The inner buoy (Fig. 6B), being in ice of 10% greater ice concentration, has more cusps, few circles, and many positions which are clumped together. Finally, the two translational examples (Fig. 6C and D) and, in particular the inner buoy (Fig. 6D), show that even in the seemingly pure translational mode, the buoys are moving in an "accordion-like" pattern containing oscillations with periods on the order of a half day.

4.3. Spectral results

The two main sources of oscillations near the half-day period are inertial oscillations and tides. Since the oscillations appear in both the trajectories and given that the buoys are regionally confined, we performed stationary periodic spectral analysis of the buoy time series during the time frame when both buoys were transmitting. Standard power spectra results (not shown) yield two dominant peaks near 12.80 and13.24 h for Buoys 1 and 2, respectively, but these have bin widths which are too wide to statistically separate the peak frequencies (Table 1). The MEM results resolve more distinct frequency peaks between the buoys (Fig. 7). The peaks are 12.87 and 13.03 h for Buoys 1 and 2, respectively. These are in close agreement with theoretical calculations for the local inertial period of each buoy (Table 1), but they are both systematically less than the theoretical values. We address this problem in Section 5.

Finally, we examine a wavelet periodogram (Fig. 8) to focus on the relationship between low-frequency events in the ice (possibly coming from the atmosphere) and energy peaks at those periods which coincide with the beginning of Event 1. The periodograms are plotted with time along the horizontal and period along the vertical to show the clustering of signal intensity as a function of both period and time. Time and frequency (inverse of period) of these

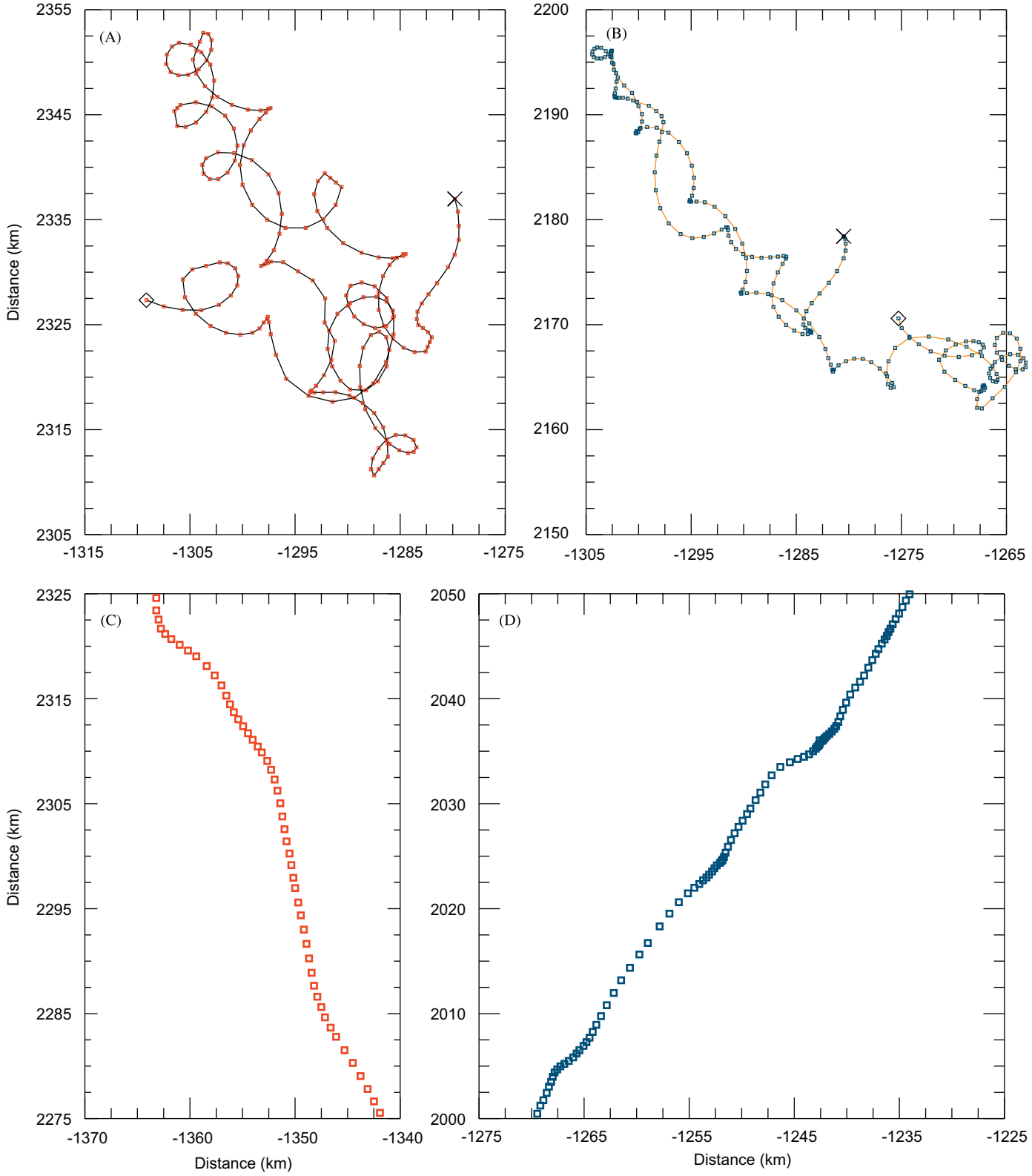

Fig. 6. Trajectory patterns. Panels (A) and (B) are subsections of buoy trajectories from day 301.25 to 310.25 in 2002. Coding of buoys matches previous figures. The start (diamond) and end ('x') of each segment also marked. Panels (C) and (D) are trajectories during notable translations from day 293.75 to 295.83 and from 355.55 to 359.60 occurring just before and after Event 2, respectively, and also near the end of each buoy lifetime when ice is both retreating southward and melting rapidly. Distances correspond with Fig. 1.

Table 1
Calculation of time coincident inertial periods

Buoy	Latitude (°S)	Theoretical inertial period (h)	Fourier power spectra (h)	Maximum entropy (h)
1 (inner)	67.01 [66.07, 67.73]	13.00 [12.93,13.09]	12.80 [12.59, 13.01]	12.87 [12.83,12.91]
2 (outer)	65.97 [65.31, 66.60]	13.10 [13.03,13.17]	13.24 [13.01,13.47]	13.03 [12.99,13.07]

Note: Mean values shown with results for minimum and maximum of the range provided in square brackets.

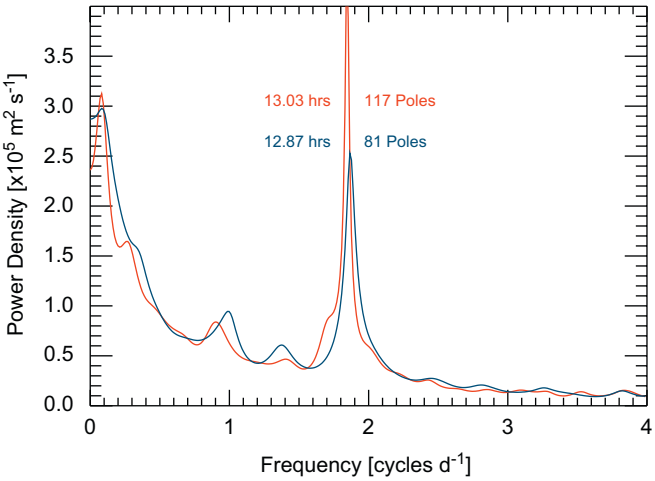

Fig. 7. Maximum entropy spectra. The velocity components of both buoys during the coincident time period (day 248.0–339.5) are used to compute the maximum entropy method (MEM) spectra at the optimal pole numbers shown. The maximum spectral bins have a frequency bin width of 0.0117 cycles per day. All results are reported using the same scheme as previous figures.

plots cannot be resolved below the criterion $\Delta t\Delta f \geqslant 1/4\pi$. This fundamental fact is responsible for the diffuse elliptical patterns in a time-frequency or time-period space in a wavelet analysis. This basic background pattern can be reproduced with a pure white noise signal, so our interests here are the locations within the periodogram which show up above the typical background pattern. In particular, a significant (above the noise) signal is the "ringing" oscillation in both u and v components which extend from the start of Event 1 to day 320, especially in the u-component near the semi-diurnal period (Fig. 8A). This time frame corresponds well with the meteorological records (Figs. 4A and 5) of sequential storms, the first of which is the strongest followed by three to five smaller low-pressure systems. In Fig. 8, the long-period contributions are centered at 10 days in the u-component but are more steady and fortnightly in the v-component (Fig. 8B). Similar signals are seen from the inner buoy periodogram but with less intensity, which we attribute to the higher ice concentration there. During Event 2, when only the inner buoy was still transmitting, we see that no low-frequency event precedes it, rather, semi-diurnal oscillations seem to be the initiator of the high energy at a 4–5 day period from day 345 to 350 coinciding with the low pressure seen at that time in Fig. 4A and the southwesterly flow of air and ice motion.

5. Discussion

High correlation in atmospheric pressure ($r^2 \geqslant 0.98$) between Rothera and both buoys (Fig. 4A) suggests reasonably uniform low-frequency meteorological forcing over the research area, which is roughly 200 km in scale (Fig. 1). However, there are lower correlations between the air temperatures (Fig. 4B) of the buoys ($r^2 = 0.93$); the outer buoy being as much as 5 °C warmer than the inner buoy. This is consistent with the outer buoy being closer to the ice edge. The Rothera station records above freezing temperatures between day 250 and 270 and has sustained daily mean temperatures above freezing from day 340 onward. The coastal station warms first, followed by the outer buoy location (near ice edge), and finally the inner buoy location, deep in the pack, (i.e. when more ice is present, the local warming rate is slower). We therefore, conclude that atmospheric forcing is well represented by the two buoys and the Rothera station with sufficiently high correlations between them to examine the low-frequency component of air-to-ice momentum transfers. We also see from Figs. 3 and 5 that all combinations of correlation between buoys and Rothera fall within the range $r^2 = 0.57$–0.89 when considering an optimal turning angle of 35° for air-to-ice momentum transfer. Further optimization of correlation is considered by imposing a time lag between Rothera and the two buoys. This effort shows small time lags with Rothera lagging between 0 and 2 h and between 3 and 6 h for the outer and inner buoys, respectively. However, these findings can only be made based on a very narrow difference in correlations relative to the no lag case (maximum correlation difference between optimal lag and zero lag is $\Delta r^2 = 0.03$). Hence, we conclude that there is no more than a 6-h lag between the meteorological station and the buoys. The lowest correlations using an optimal turning angle are the v components of both buoys relative to Rothera ($r^2 = 0.56$ and 0.57, Fig. 5) while the highest correlations are between the buoys' v components ($r^2 = 0.81$, Fig. 3 and $r^2 = 0.89$, Fig. 5). Recalling that the v component is oriented parallel to the coast, this finding suggests a correlated response of the migration and breakup of the ice in addition to low-frequency wind processes. These results corroborate earlier findings by Colony and Thorndike (1980) discussed in Section 1. The difference between Rothera and buoys in the lower v correlations suggests a shear between meteorological station and buoys. This agrees well with findings reported in Beardsley et al. (2004) and Klinck et al. (2004) regarding the strong coastal current found in Marguerite Bay.

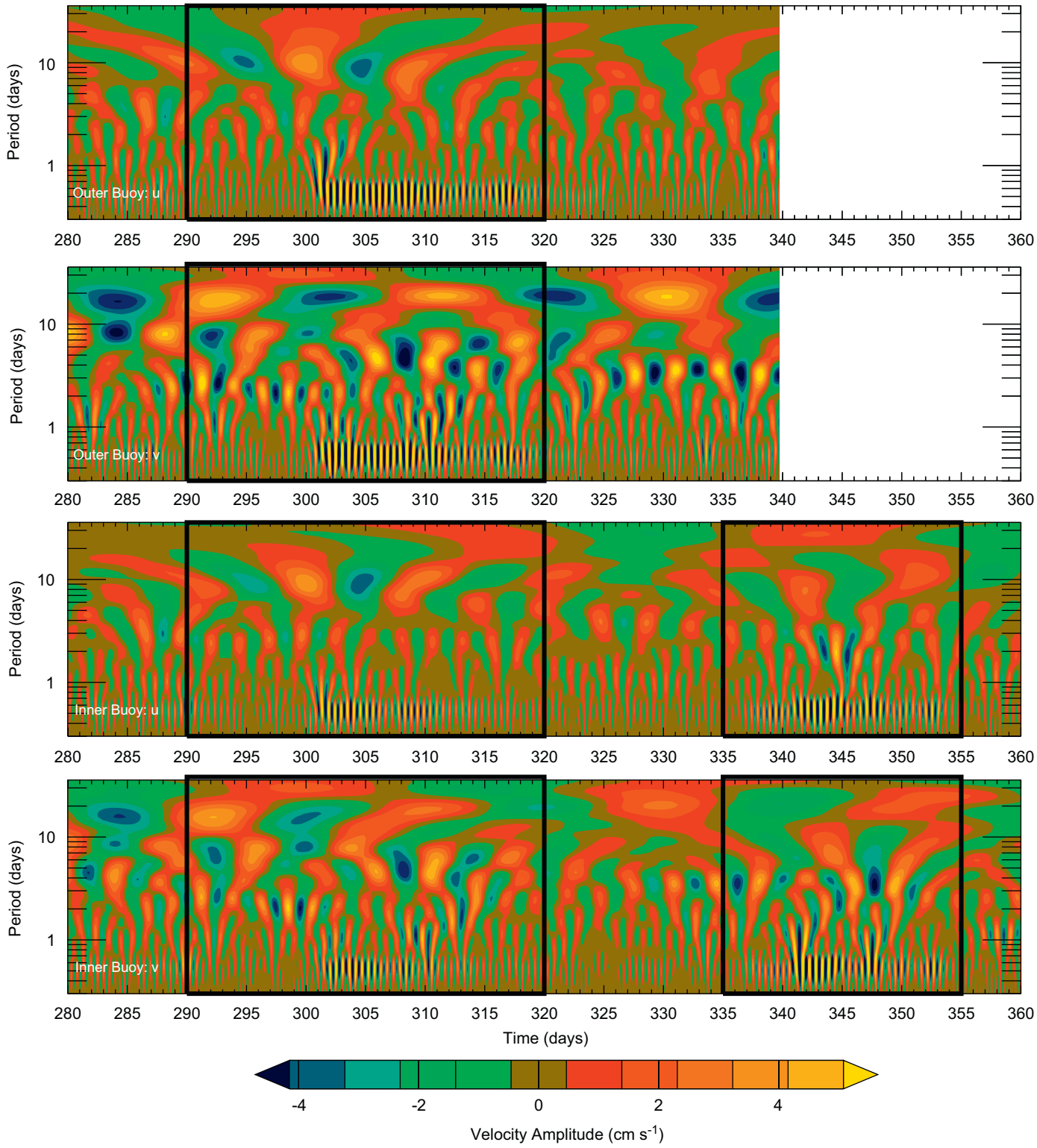

Fig. 8. Wavelet periodogram. Ice velocity components u and v are oriented perpendicular and parallel to the coastline east of these buoys. The outer buoy (Buoy 2) is closest to the ice edge while the inner buoy (Buoy 1) is deeper in the pack ice. Semi-diurnal oscillations during Events 1 and 2 are seen as the high amplitude oscillations near the half-day period starting around day 301 and 339, respectively. Boxes surround longer time segments in the vicinity of these events.

5.1. Near-inertial motion

The MEM method reveals a strong, predominantly inertial, signal but there is also a slight shift in the computed frequency relative to theoretical calculations (Table 1). There are two possibilities for this shift. One is a possible tidal influence. Evidence for this comes from three different parts of the signal. First, there is a prominent

Table 2
Critical latitudes

Tidal name	Relative strength	Tidal period	Critical latitude
Semi-diurnal (S2)	47	12.00	85.76
Principal lunar (M2)	100	12.42 (five bins from lowest MEM range)	74.42
Larger lunar elliptic (N2)	19	12.66 (two bins from lowest MEM range)	70.96

Note: Equation to determine critical latitude is $\phi = \sin^{-1}(f/2\Omega)$, where f is the Coriolis parameter and $\Omega = 1/86164$ or the inverse of one sidereal day in units of inverse seconds. Latitude (ϕ) given in radians in this equation and must be converted to degrees for table.

fortnightly (possibly M_f) signal in the v component in the wavelet periodogram (Fig. 8). Second, there is a small diurnal peak in the power spectra of the inner buoy. Third, there are two critical latitudes (latitudes where a tidal frequency equals the local inertial frequency), M_2 and N_2, that are close enough in period to influence the calculation (Table 2) as evidenced by the fact that the inner buoy (which is closer to the critical latitudes) deviates from the inertial period more than the northerly buoy.

A second possibility for the discrepancies in Table 1 may result from the design of our experiment; namely, we are using drifting buoys that are subject not only to local oscillations but also ambient horizontal currents which can shift the inertial frequency through relative vorticity considerations (van Meurs, 1998). This is also a strong possibility given the translational drift of the ice parallel to the nearby coastline and the strong coastal current in this region. Mathematically, this is written as $f' = f + ix$ where f is the local inertial frequency and ix is the relative vorticity of the ambient flow, which gives rise to f', the shifted oscillation frequency.

5.2. Impacts of high-frequency ice motion

The task of clearly distinguishing tides and inertial oscillations near critical latitudes remains an unsolved problem within the field of physical oceanography though there are some very useful techniques for statistically distinguishing between them using harmonic analysis even for drifting buoys (Pease et al., 1995). However, these methods do not solve the problem of frequency shift due to current effects. In short, the problem essentially remains an active area of research. For this experiment, our findings show that the buoys are sufficiently north from the critical latitudes that either tidal effects and/or currents may be responsible for a shift in frequency, but that contribution is small. The dominant signal is inertial and influenced by wind forcing or differential wind stress with the ice floes responding as rigid bodies upon a reduced frictional surface on a rotating planet as so clearly demonstrated by Hunkins (1967) and McPhee (1978).

Beardsley et al. (2004) and Howard et al. (2004) both report near-inertial oscillations in the mixed layer of the ocean from surface drifters and subsurface measurements, respectively, during this experiment even in the absence of sea-ice. Hence, the region is affected by strong near-inertial motion whether ice is present or not. Unlike the ocean, however, the sea-ice is a solid material. In the autumn, sea-ice has a strong structural integrity with grains forming first in a random orientation and later as columnar ice. There are brine channels that form within the ice during the formation process, which serve as habitats for a small number of organisms to overwinter. Hence, these pores and brine channels form a floating habitat.

As presented in Section 1, with the returning sunlight in spring, the ice begins to warm, melt, and decay. At the same time, organisms within the ice begin utilizing the sunlight as a resource for primary productivity. This, in turn, serves as a food source for the overwintering zooplankton. A feedback process ensues with the pore microstructure decaying further as the biological productivity increases. The living organisms within the ice have a lower albedo than the ice. This leads to a positive feedback for productivity and a negative feedback for sea-ice structural integrity. These microscale processes only occur together under springtime conditions. The decreasing structural integrity at the microscale facilitates the break up of large ice floes into smaller plates and eventually small floes. This, in turn, increases surface area to facilitate further warming and advance melting. Hence, under strong pulsing wind conditions and resulting strong semi-diurnal oscillations, the reduced ice strength enhances melting resulting in decreased ice concentration—a positive feedback mechanism for increasing mixing length scales. From a biological perspective, this leads to a maximum in habitat mobility at the start of a positive feedback primary productivity process. Therefore, the combination of decaying ice microstructure and strong mesoscale oscillatory motion set the conditions for an important biophysical relationship, namely, sea-ice as a seeding mechanism (i.e. the sea-ice moves, decays, and disburses its overwintering inhabitants over vast regions on a relatively short time scale of days to a few short weeks).

This multi-scale seeding mechanism only exists in springtime with the returning sunlight. This connection during the spring months means that sea-ice plays an important role in the preconditioning of springtime high biomass productivity. Queries within the biological oceanographic community indicate that the consideration of sea-ice as a seeding agent for primary productivity through mesoscale semi-diurnal oscillations has not been examined as a phenomenon.

6. Concluding remarks

In this study, two ice-drifting buoys separated by 1° latitude reveal two key types of motion; low-frequency translational motion driven by winds and topographic steering (transport), and semi-diurnal oscillatory motion (mixing). The oscillations are isolated with spectrally distinct near-inertial periods. The oscillations are examined with respect to kinematic processes relevant to ice breakup. A combination of circular trajectories, semi-circular oscillations with compressed trajectory cusps, and "accordion-like" compressions along straight-line trajectories are found over the lifetime of both buoys (several months). Examining two episodes, we find evidence to support a hypothesis that pieces of sea-ice (i.e. individual ice floes) physically mix the water while they are decaying and melting. These processes of decay and melt contribute to the springtime removal of the sea-ice cover.

Just as tides are key contributors to vertical and horizontal mixing processes within the ocean (Munk and Wunsch, 1998), we find that inertial oscillations dominate surface and near-surface vertical and horizontal mixing with those processes being enhanced when sea-ice is included as an additional mechanical stirring mechanism. This makes sense in light of the physical origin of tides and inertial oscillations as discussed at the very beginning of this paper. From this physical perspective, we expect inertial oscillations to dominate sea-ice motion. Since sea-ice floes are solid body structures, inertial motion should clearly dominate in the inertial range under low ice concentration conditions ($<80\%$). It is further clear from a description of tides (from the ocean) and inertial oscillations (of sea-ice), why regions such as the Weddell Sea become source regions for bottom-water production as a result of resonant tidal and inertial oscillations and their associated mixing processes. Finally, from a biological perspective, it is particularly important to realize that sea-ice floes are not only structures for biological communities to survive in, but also essential for transportation, dispersion, and mechanics/thermodynamic mixing. In this regard, sea-ice is a vital water habitat, albeit in the frozen constituent form, and therefore an essential component for the abundant biological productivity found in the polar regions.

Acknowledgments

This work was funded by the National Science Foundation, Office of Polar Programs Antarctic Program. We thank the UK Meteorological Office for sustaining a wonderful database of Antarctic weather stations, and NASA and NSIDC for access to SSM/I sea-ice concentrations. Much thanks to Bruce Elder and Keran Claffey of CRREL for deploying the buoys. Also thanks goes to Andreas Muenchow and Andrey Prosutinsky for their insight on ocean tides, ocean inertial effects, and the current understanding of these phenomena within the polar oceanographic community. Thanks also goes to Carin Ashjian, Rolf Gradinger, Sharon Smith, and Walker Smith for their personal communications regarding polar biological ecosystems. Finally, thanks go to the two anonymous reviewers whose comments improved the paper further. Graphics for this paper were generated using PV-Wave®. This is US GLOBEC contribution number 515.

References

Ackley, S.F., Sullivan, C.W., 1994. Physical controls on the development and characteristics of Antarctic sea ice biological communities—a review and synthesis. Deep-Sea Research I 41 (10), 1583–1604.

Ackley, S.F., Weeks, W.F., 1990. Sea ice properties and processes. In: Proceedings of the W. F. Weeks Sea Ice Symposium, US Army Cold Regions Research and Engineering Laboratory, 299p. CRREL Report No: M 90–01.

Beardsley, R.C., Limeburner, R., Owens, W.B., 2004. Drifter measurements of surface currents near Marguerite Bay on the western Antarctic Peninsula shelf during austral summer and fall, 2001 and 2002. Deep-Sea Research II 51, 1947–1964.

British Antarctic Survey Meteorological Office, 2005. Website 〈http://www.antarctica.ac.uk/cgi-bin/metdb-form1.pl?table_prefix=U_WMC,U_MET&acct=cmet〉.

Colony, R., Thorndike, A.S., 1980. The horizontal coherency of the motion of summer Arctic sea ice. Journal of Physical Oceanography 10 (8), 1281–1289.

Emery, W.J., Thomson, R.E., 1997. Data Analysis Methods in Physical Oceanography. Elsevier Science Inc., New York, 634pp.

Foldvik, A., Gammelsrød, T., 1990. Notes on Southern Ocean hydrography, sea ice and bottom water formation. Palaeogeography Paleoclimatology Paleoecology 67, 3–17.

Geiger, C.A., Drinkwater, M., 2005. Coincident buoy- and SAR-derived surface fluxes in the western Weddell Sea during Ice Station Weddell 1992. Journal of Geophysical Research 110, C04002.

Geiger, C.A., Ackley, S.F., Hibler III, W.D., 1998a. Sea ice drift and deformation processes from field measurements in the Western Weddell Sea during 1992. In: Jeffries, M.O. (Ed.), Antarctic Sea Ice Processes, Interactions and Variability, Antarctic Research Series, vol. 74. AGU, Washington, D.C, pp. 141–160.

Geiger, C.A., Hibler III, W.D., Ackley, S.F., 1998b. Large-scale sea ice drift and deformation: comparison between models and observations in the western Weddell Sea during 1992. Journal of Geophysical Research. Special Issue on Sea Ice Mechanics 103 (C10), 21893–21913.

Heil, P., Hibler, W.D., 2002. Modeling the high-frequency component of Arctic sea ice drift and deformation. Journal of Physical Oceanography 32 (11), 3039–3057.

Hibler III, W.D., Roberts, A., Heil, P., Proshutinsky, A.Y., Simmons, H.L., Lovick, J., 2006. Modeling M2 tidal variability in Arctic sea-ice drift and deformation. Ann. Glaciol. 44, 418–428.

Hofmann, E.E., Wiebe, P.H., Costa, D.P., Torres, J.J., 2004. An overview of the Southern Ocean Global Ocean ecosystems dynamics program. Deep-Sea Research II 51, 1921–1924.

Howard, S.L., Hyatt, J., Padman, L., 2004. Mixing in the pycnocline over the western Antarctic Peninsula shelf during SO GLOBEC. Deep-Sea Research II 51, 1965–1979.

Hunkins, K., 1967. Inertial oscillations of Fletchers Ice Island (T-3). Journal of Geophysical Research 72 (4), 1165–1174.

Klinck, J.M., Hofmann, E.E., Beardsley, R.C., Salihoglu, B., Howard, S., 2004. Water-mass properties and circulation on the west Antarctic Peninsula Continental Shelf in austral fall and winter 2001. Deep-Sea Research II 51, 1925–1946.

Kwok, R., Cunningham, G.F., Hibler, W.D., 2003. Sub-daily sea ice motion and deformation from RADARSAT observations. Geophysical Research Letters 30 (23), 2218.

Lütkepohl, H., 1985. Comparison of criteria for estimating the order of a vector autoregressive process. Journal of Time Series Analysis 6 (1), 35–52.

McPhee, M.G., 1978. Simulation of inertial oscillations in drifting pack ice. Dynamics of Atmospheres and Oceans 2 (2), 107–122.

Munk, W.H., Wunsch, C., 1998. Abyssal recipes II: energetics of tidal and wind mixing. Deep-Sea Research I 45, 1977–2010.

NSIDC Website, 2005. 〈http://sidads.colorado.edu/pub/DATASETS/PASSIVE_MICROWAVE/POLAR_STEREO/DATA/SEAICE/SMMR-SSMI/BOOTSTRAP/DAILY/SOUTHERN/〉 (documentation at 〈http://nsidc.org/data/docs/daac/nsidc0079_bootstrap_seaice.gd.html〉).

Pease, C.H., Turet, P., Pritchard, R.S., 1995. Barents Sea tidal and inertial motions from Argos ice buoys during the Coordinated Eastern Arctic Experiment. Journal of Geophysical Research 100 (C12), 24705–24718.

Pond, S., Pickard, G.L., 1983. Introductory Dynamical Oceanography, second ed. Pergamon Press, New York, 329pp.

Press, W.H., Flannery, B.P., Teukolsky, S.A., Vetterling, W.T., 1990. Fourier Transform Spectral Methods, in Numerical Recipes Fortran Version. Cambridge University Press, New York (pp. 381–453, Chapter 12).

Roberts, J., Roberts, T.D., 1978. Use of the Butterworth Low-Pass Filter for Oceanographic Data. Journal of Geophysical Research 83 (C11), 5510–5514.

Sedwick, P.N., DiTullio, G.R., 1997. Regulation of algal blooms in Antarctic shelf waters by the release of iron form melting sea ice. Geophysical Research Letters 24, 2515–2518.

Smith Jr, W.O., Gordon, L.I., 1997. Hyperproductivity of the Ross Sea polynya during austral spring. Geophysical Research Letters 24, 233–236.

Smith Jr, W.O., Marra, J., Hiscock, M.R., Barber, R.T., 2000. The seasonal cycle of phytoplankton biomass and primary productivity in the Ross Sea, Antarctica. Deep-Sea Research II 47, 3119–3140.

Van Meurs, P., 1998. Interaction between near inertial mixed layer currents and the mesoscale: the importance of spatial variabilities in the vorticity field. Journal of Physical Oceanography 28, 1363–1388.